

Electronic Supplementary Information

Inorganic Separators Enable significantly suppressed Polysulfide Shuttle towards High-Performance Lithium-Sulfur Batteries

Hongtao Qu,^{a,b,‡} Jiangwei Ju,^{a,‡} Bingbing Chen,^{a,‡} Nan Xue,^{a,b} Huiping Du,^{a,b} Xiaoqi Han,^{a,b} Jianjun Zhang,^a Gaojie Xu,^a Zhe Yu,^a Xiaogang Wang,^a and Guanglei Cui^{a}*

^a Qingdao Industrial Energy Storage Technology Institute, Qingdao Institute of Bioenergy and Bioprocess Technology, Chinese Academy of Sciences. Qingdao 266101, P. R. China. E-mail: cuigl@qibebt.ac.cn

^b University of Chinese Academy of Sciences, No.19A Yuquan Road, Beijing, China, 100049

[‡] These authors contribute equally to this work.

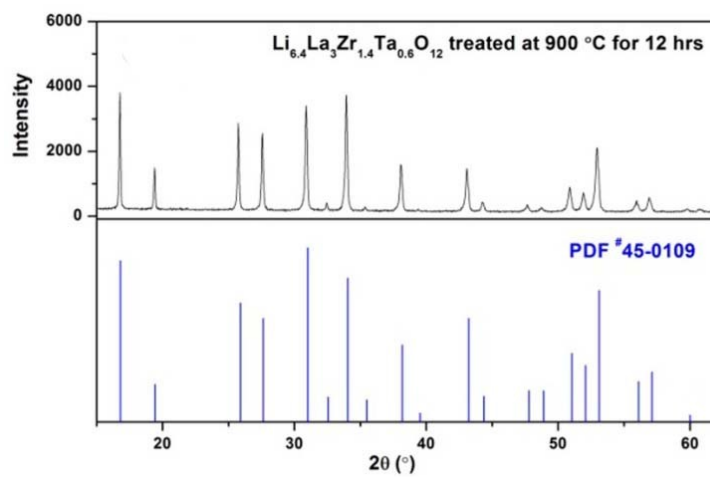


Fig. S1. X-ray diffraction (XRD) patterns of as-prepared LLZTO.

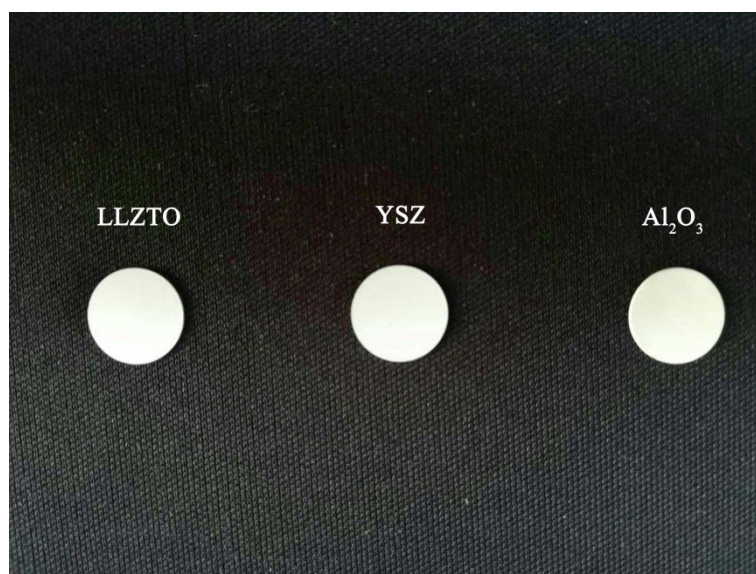


Fig. S2. Digital images of inorganic separators

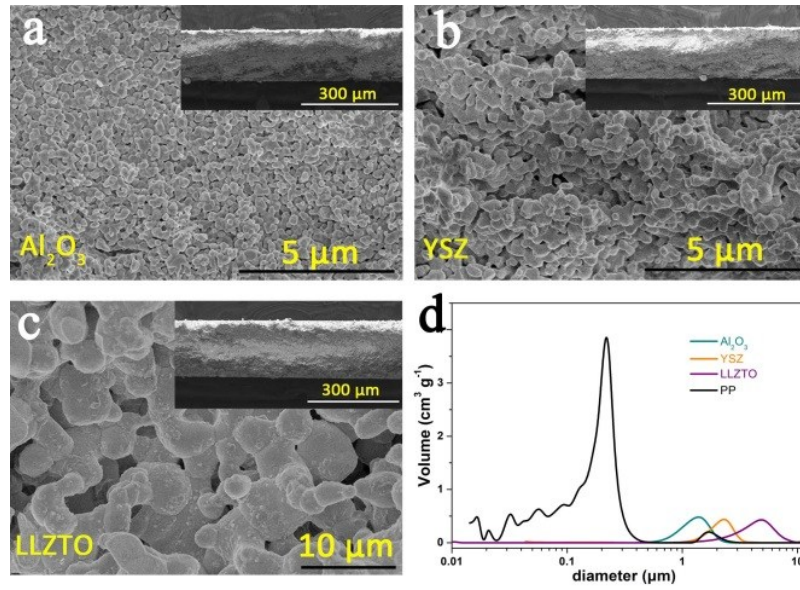


Fig.S3. Scanning electron microscopy (SEM) images in cross section of (a) Al₂O₃, (b) YSZ and (c) LLZTO.(d) Pore size distributions of PP, LLZTO, YSZ and Al₂O₃.

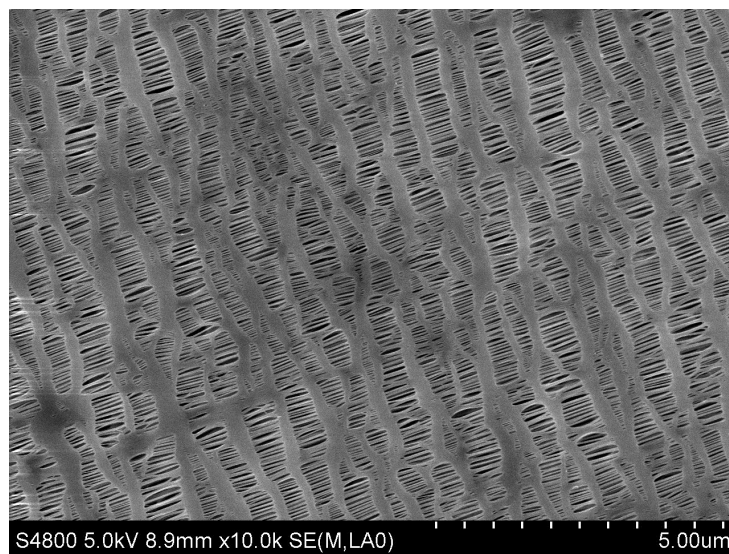


Fig. S4. SEM images of commercial PP separator (Celgard 2500).

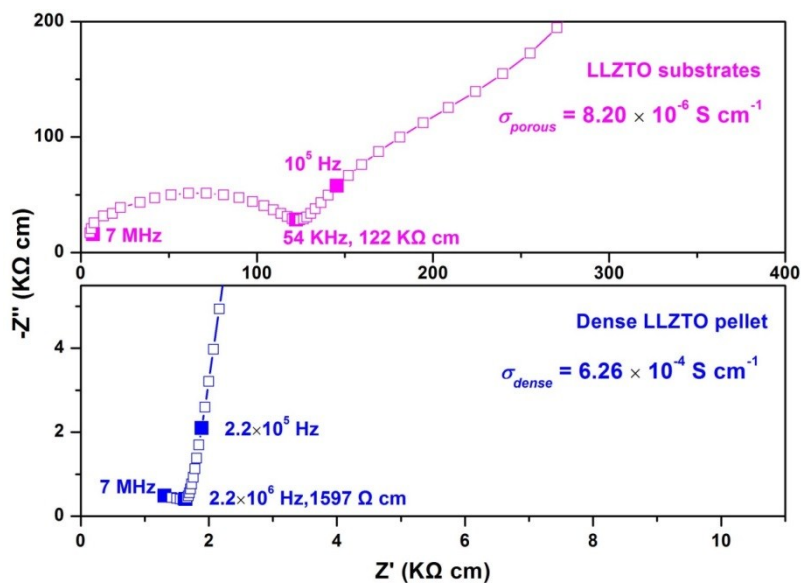


Fig. S5. Ion conductivities of porous and dense LLZTO pellet.

The EIS of LLZTO measured at room temperature ($\sim 25 \text{ }^\circ\text{C}$) are shown in Fig. S5. Both dense and porous LLZTO plots show semicircles at high frequencies, connected with a remarkable diffusion tail at medium-low frequencies, agreeing well with the previous reports.^{1, 2} According to references analysis, the intercept of the semicircle with the Z' -axis represents the total or Ohmic resistance. The values are marked in Fig. S5. The estimated conductivity of the dense LLZTO pellets, σ_{dense} is about $6.26 \times 10^{-4} \text{ S cm}^{-1}$ at room temperature, which is a relatively high value compared with previous literatures. The high ionic conductivity is due to the dense crystal material with low grain boundaries benefits ion transportation.² After 'fermentation', this value decreases to $8.20 \times 10^{-6} \text{ S cm}^{-1}$ for porous LLZTO substrate, σ_{porous} . This is unable to operate the Li-S battery at room temperature. Generally, the interfacial chemistry of garnet electrolyte and electrodes are also identified as the major challenges for the application of solid electrolyte. In view of this case, the use of liquid electrolyte is still requisite.

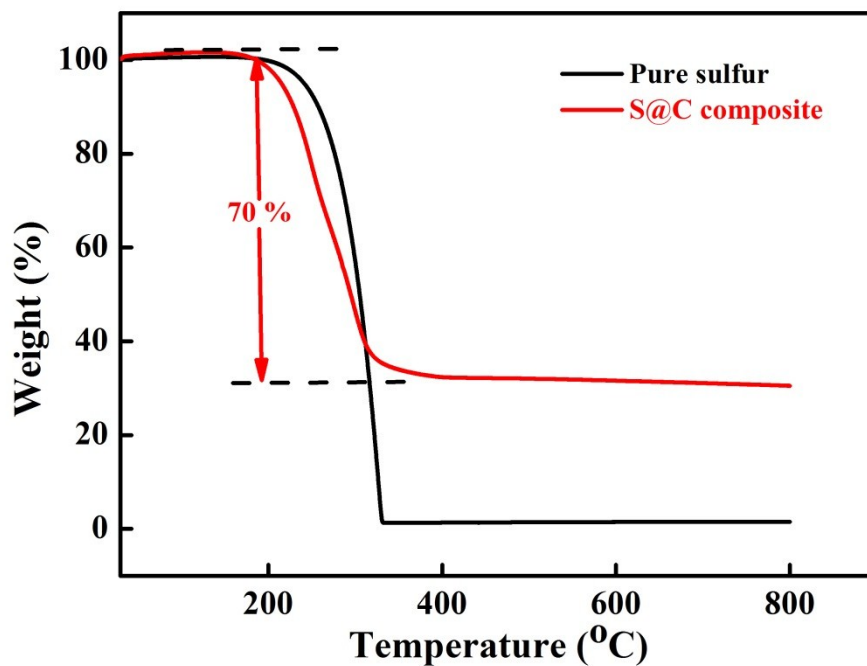


Fig. S6. TGA curves of S@CNT composite and pure sulfur with a heating rate $10\text{ }^{\circ}\text{C min}^{-1}$ under nitrogen atmosphere. From the TGA curves, the sulfur content was determined to be 70 % by weight.

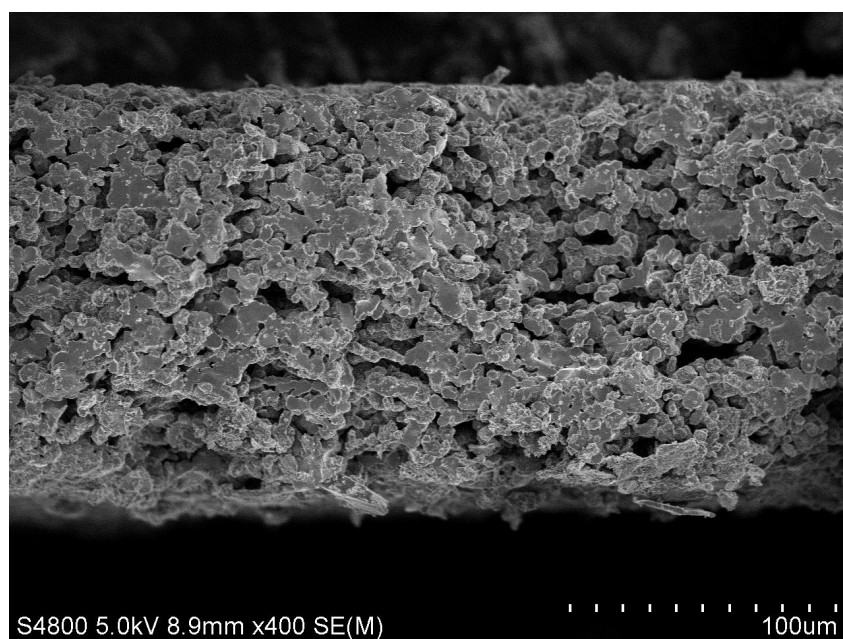


Fig. S7. SEM image of 150 μm -thick LLZTO separator

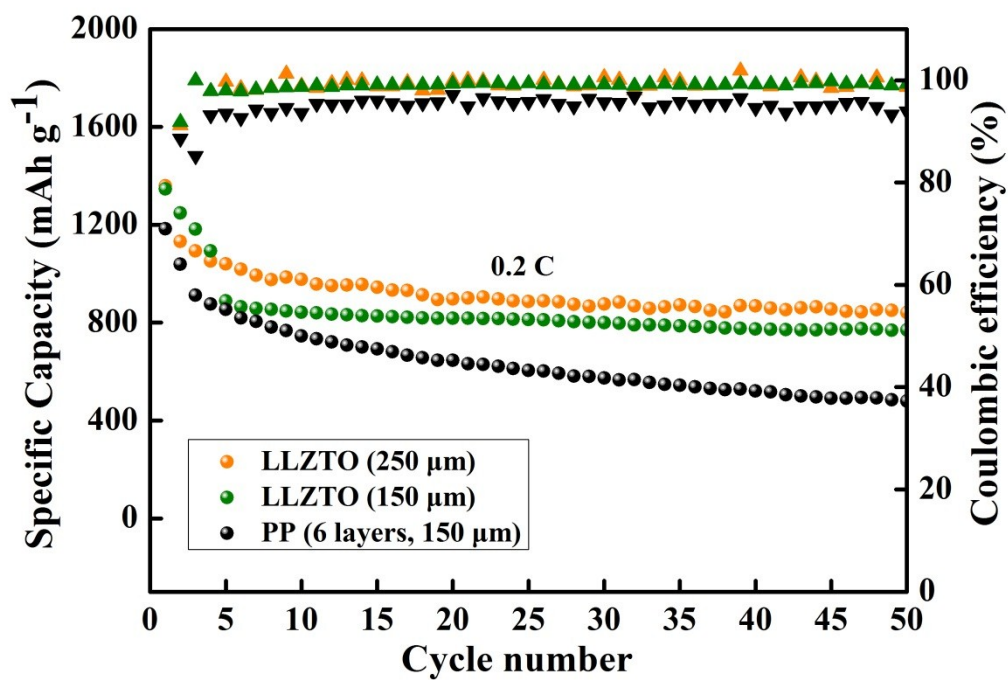


Fig. S8 Cycling behaviors of Li-S batteries using separators with different thickness.

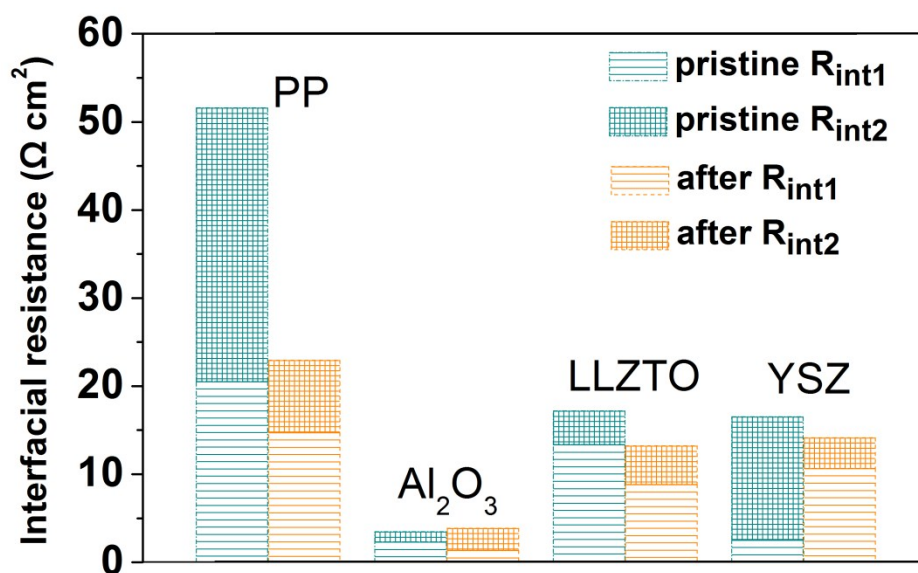


Fig.S9. The evolution of interfacial resistance of Li-S batteries based on different separators.

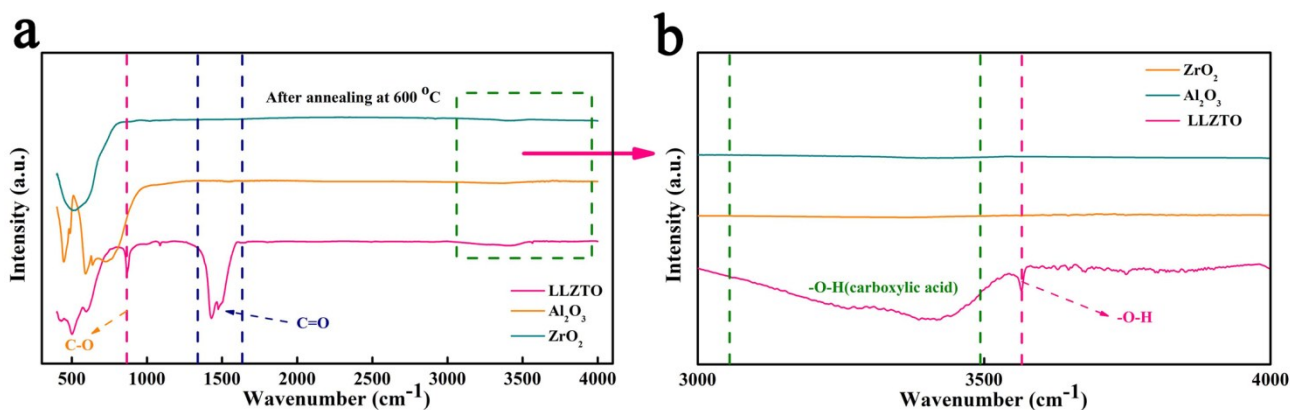


Fig.10. (a) FT-IR spectrum of LLZTO, YSZ and Al₂O₃. (b) Magnified part of the area noted by green dash square in (a).

Generally, the Li₇La₃Zr₂O₁₂ family shows strong basicity which is vulnerable to attack from vapor water and CO₂. It has been proven that the H⁺ enter the lattice and replace the Li⁺, leaving the hydroxyl on the grain surface to form hydroxides, such as LiOH or La(OH)₃.^{3,4} Fig. S10a shows the FTIR spectra of LLZTO, YSZ, Al₂O₃ powder that are used to prepare corresponding separators. To eliminate the influence of moisture (see Fig. S11), the three powders were annealed at 600 °C for 6 hrs. The peaks around 864 cm⁻¹ and 1438 cm⁻¹ confirm the formation of Li₂CO₃ due to unavoidable reaction between LLZTO and CO₂ in the preparation process of LLZTO. The region noted by green dash square is magnified in Fig. S10b. The appearance of sharp peak at around 3566 cm⁻¹ gives an evidence for the presence of OH stretching vibration.^{5, 6} However, no signals of carbonates or hydroxyl can be recognized from the FTIR spectra of YSZ and alumina separators. The hydroxyl group has been studied to be in the position to effectively immobilize the polysulfide shuttle.⁷ Consequently, the LLZTO separator based Li-S battery stands out from the batteries employing YSZ, Al₂O₃, and PP separators.

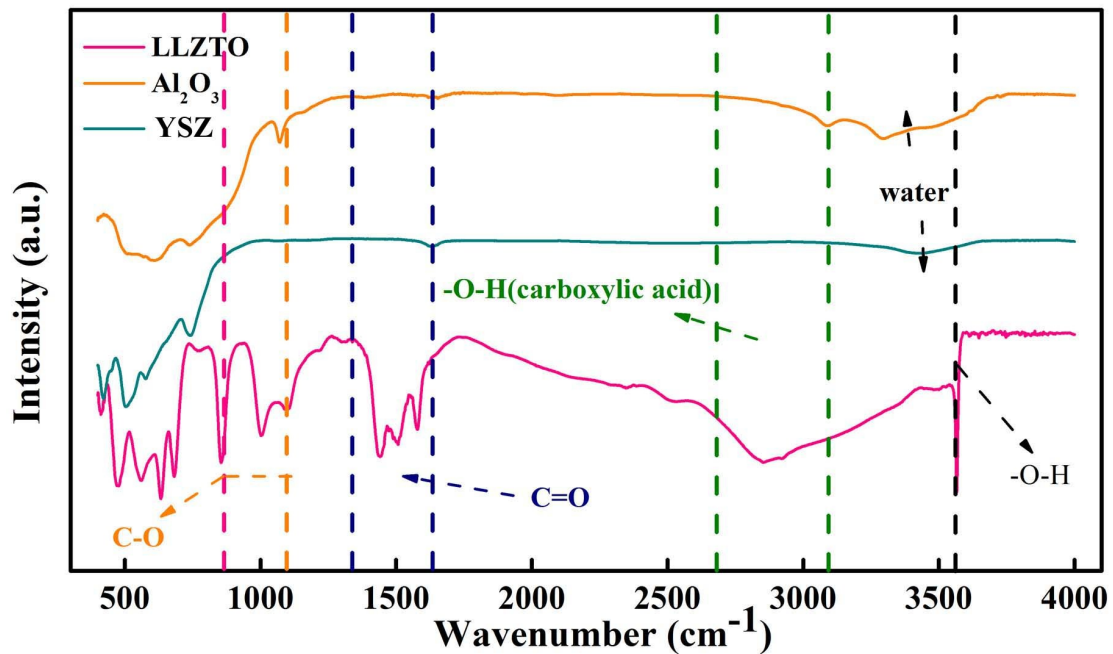


Fig. S11. FT-IR spectrum of LLZTO, Al₂O₃ and YSZ without heat treatment.

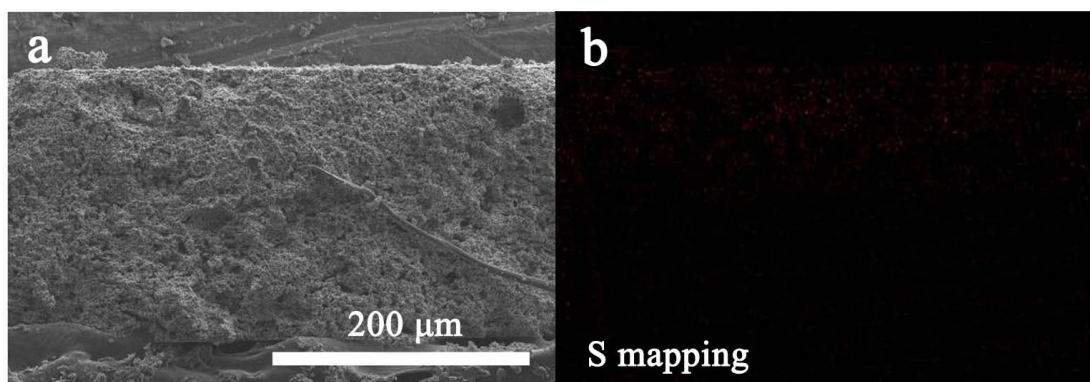


Fig. S12. (a) SEM image of cycled LLZTO separator and (b) corresponding S mapping

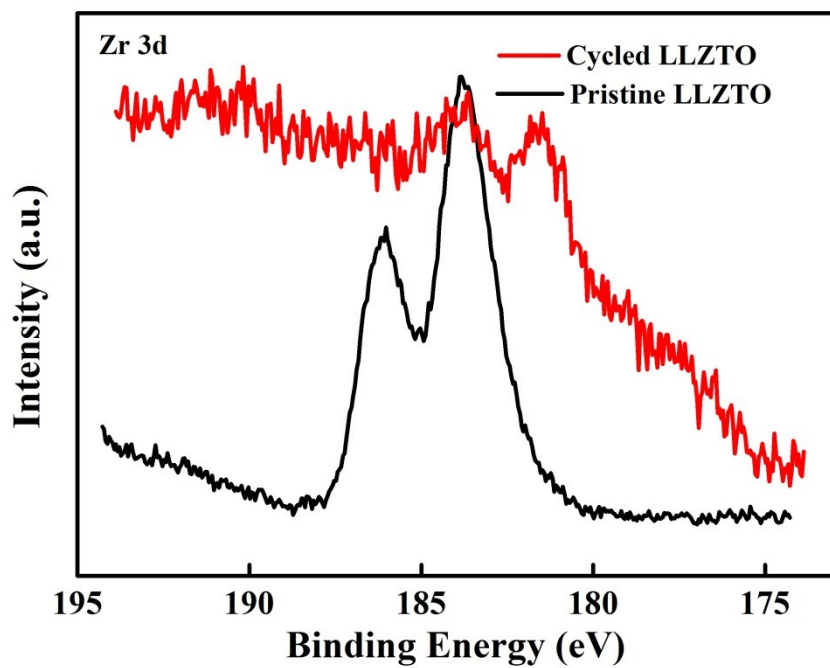


Fig. S13. High resolution XPS spectra of Zr 3d in LLZTO separator.

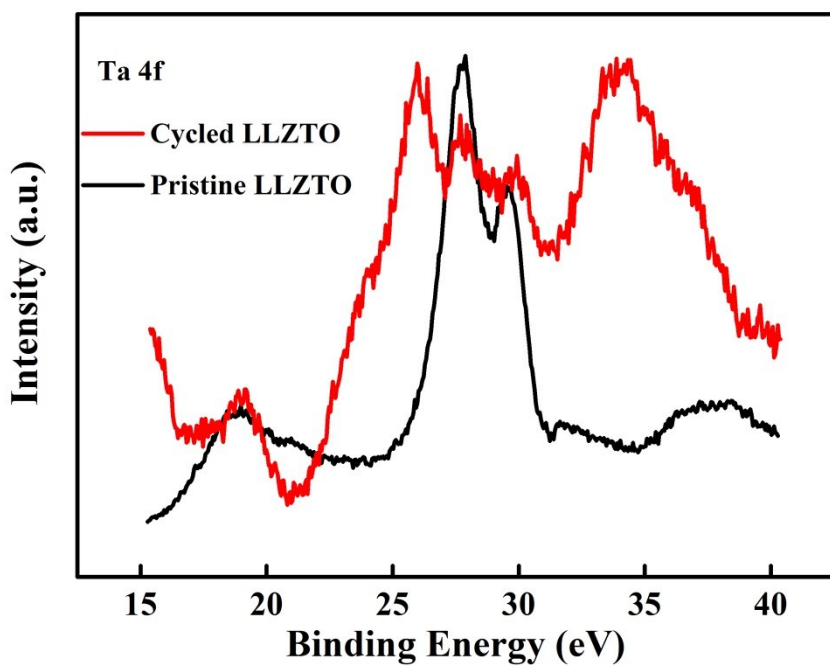


Fig. S14. High resolution XPS spectra of Ta 4f in LLZTO separator.

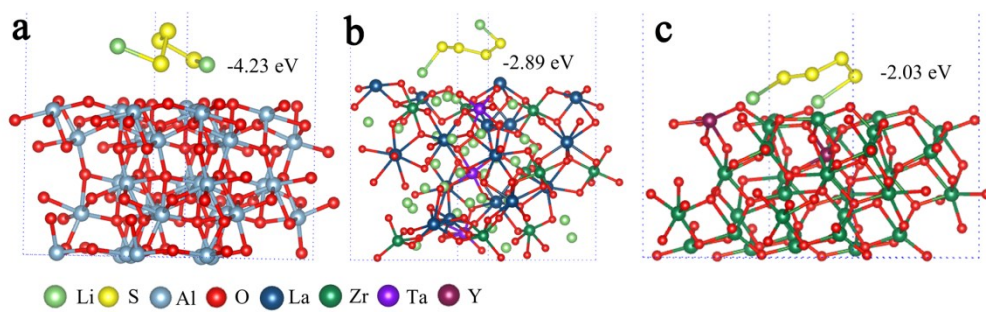


Fig.15. The adsorption energy of Li_2S_4 on (a) Al_2O_3 , (b) LLZTO and (c) YSZ.

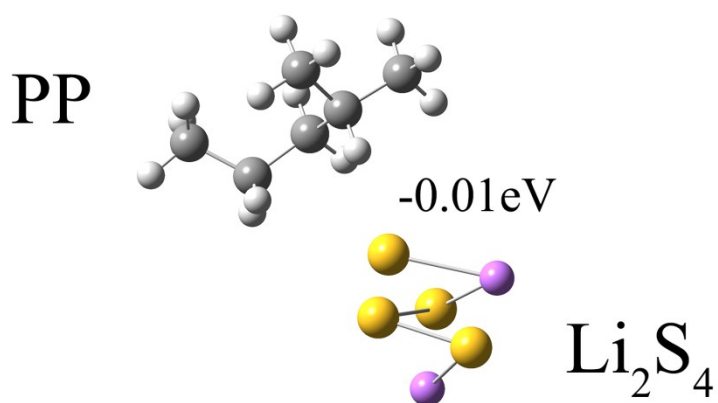


Fig.S16 The adsorption energy of Li_2S_4 on PP separator

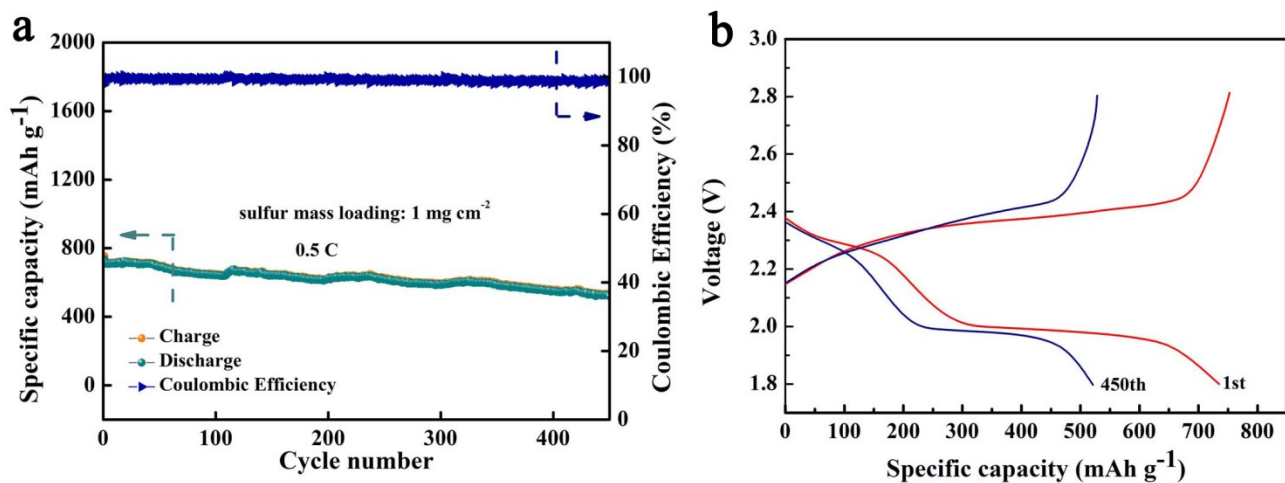


Fig. S17. (a) Long-term cycling performance of Li-S battery based on YSZ separator and (b) corresponding charge-discharge curves at different cycles.

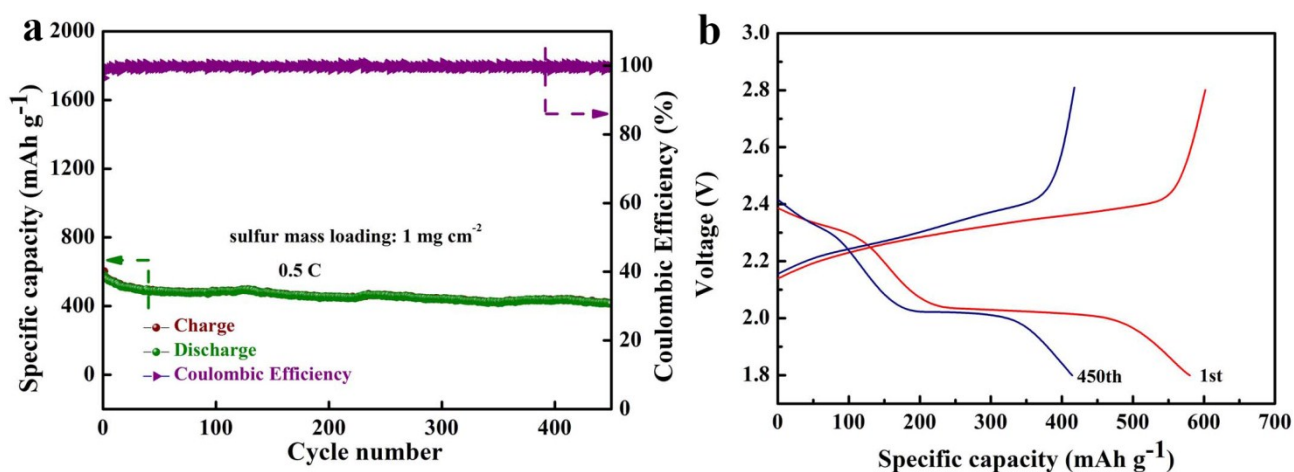


Fig. S18. (a) Long-term cycling performance of Li-S battery based on Al_2O_3 separator and (b) corresponding charge-discharge curves at different cycles.

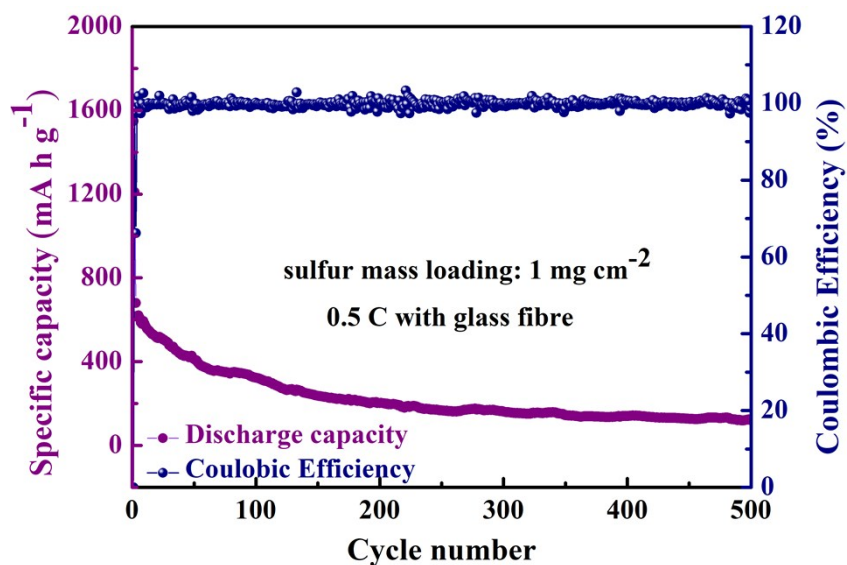


Fig.S19. Cycling behavior of Li-S battery with glass fibre.

As is shown in Fig.S19, Li-S battery with glass fibre was tested at 0.5 C with sulfur mass loading of 1 mg cm^{-2} , Li-S battery delivered an initial capacity of 750 mA h g^{-1} . In the subsequent cycles, Li-S battery with glass fibre showed fast capacity decay. After 500 cycles, the remained capacity was less than 200 mA h g^{-1} . The possible reason for such dramatical capacity decay was the large amount dissolution of polysulfide, causing large loss of active materials. When glass fibre was used, much more electrolyte was added into the battery. As the loose structure of glass fibre failed to mitigate the dissolution and migration of polysulfide species. As a result, the battery with glass fibre showed continuous capacity decay in the charge/discharge process.

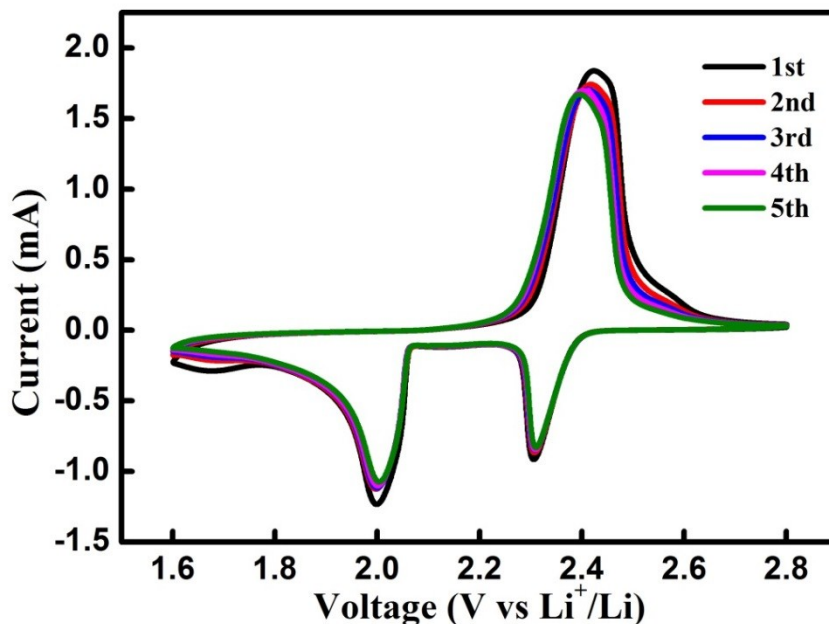


Fig. S20. Cyclic voltammetry (CV) profile of L-battery with a scan rate of 0.1 mV S^{-1} .

The CV curves of the first five circles at a scan rate of 0.1 mV S^{-1} in the range 1.6 - 2.8 V are shown in Fig. S20. Two typical cathodic peaks can be distinctly found at about 2.31 and 2.0 V (vs Li/Li⁺), which correspond to the transformation of S₈ to high-order Li₂S_n and further reduction to Li₂S₂/Li₂S, respectively. Likewise, two lapped anodic peaks located at around 2.4 V could be ascribed to the formation of high-order LiPSs and sulfur. These CV peaks suggest typical electrochemical processes of Li-S batteries.^{8, 9} Observing carefully, the cathodic and anodic peaks shift oppositely along with cycling. The cathodic peaks, for example, shift from 2.42 to 2.39 and 2.45 to 2.43 V, respectively. The anodic peaks, conversely, shift from 1.99 to 2.00 and 2.30 to 2.31 V, respectively. This phenomenon implies the promoted reversibility of the batteries with LLZTO separators. Besides, the highly overlapped CV plots demonstrate the outstanding durability of these batteries.

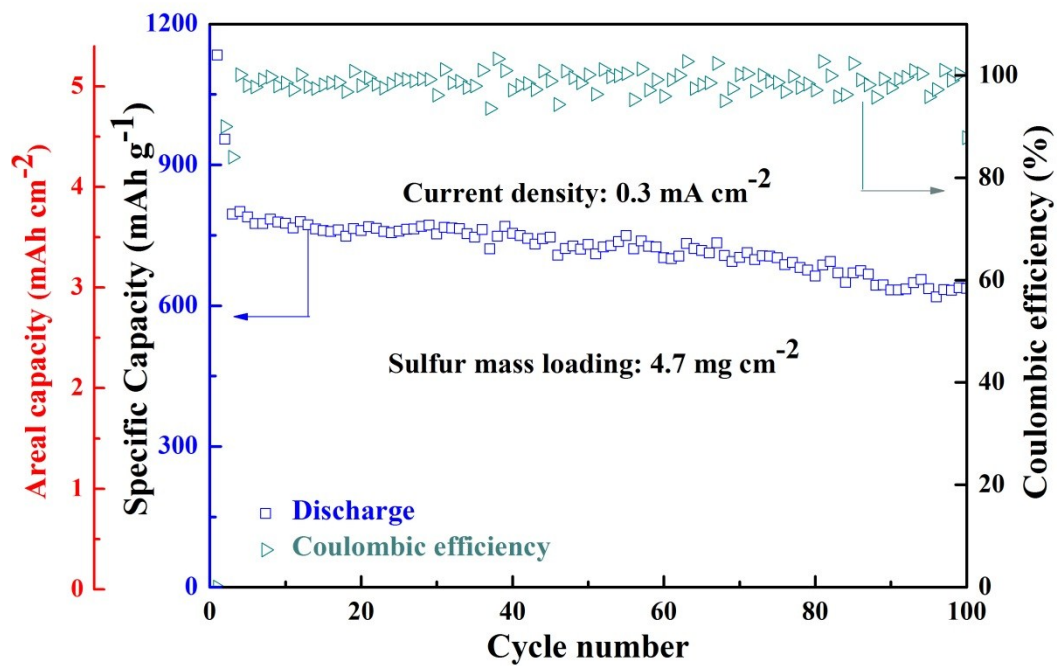


Fig. S21. Cycling behavior of Li-S battery using LLZTO separator with high sulfur mass loading

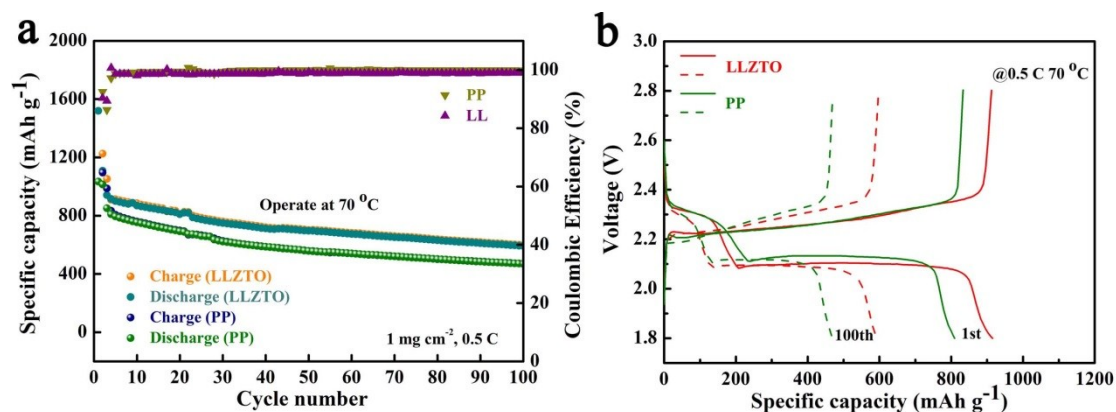


Fig. S22. (a) Cycling behavior comparisons of LLZTO- and PP-based battery at 70 °C. (b)

Corresponding discharge-charge curves.

The heat resistance is of great importance in the practical application of Li-S battery, particularly in harsh conditions.¹⁰ Generally, the conventional PP separator is also heat-shrinkable above 80 °C. The poor thermal endurance of conventional PP separator will cause serious potential safety hazard. In contrast, the inorganic separators can keep thermal integrity even at elevated temperature. Fig. S22a shows the cycling behavior comparison of Li-S batteries with PP and LLZTO separator operating at 70 °C. LLZTO based battery delivers a high initial discharge capacity of 915 mA h g⁻¹ at 0.5 C and keeps at 600 mA h g⁻¹ after 100 cycles. Meanwhile, the PP based battery shows a capacity of 809 mA h g⁻¹ and falls to 469 mA h g⁻¹. The dramatic capacity drop of PP-based battery is caused by the rapid diffusion of soluble polysulfides at the elevated temperature. These results indicate that the use of LLZTO separator is benefitted to improve the performance of the Li-S battery when operated at high temperature.

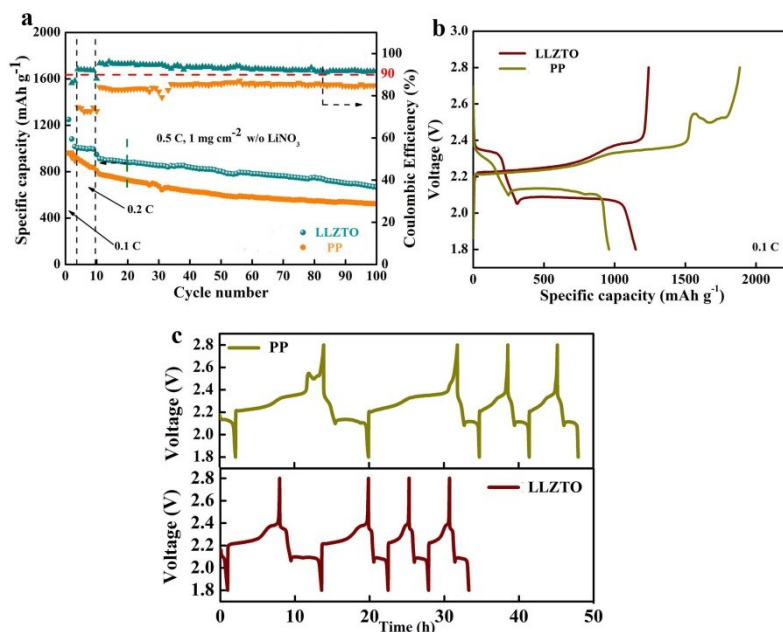


Fig. S23. (a) Cycling performance of LLZTO- and PP-based batteries without LiNO_3 additive and (b) corresponding charge-discharge curves of the first cycle.(c) Charge-discharge curves of LLZTO- and PP-based batteries in the first several cycles (0.1 C for the first 3 cycles and 0.2 C for the subsequent cycles).

It is well known that lithium nitrate (LiNO_3) is a pivotal additive in Li-S battery electrolyte system. It can protect the Li metal anode by formation of robust solid electrolyte interface (SEI) film, preventing Li metal from being eroded by the shuttled polysulfides.¹¹ However, LiNO_3 is found to be irreversibly reduced on cathode side progressively when the discharge cutoff is lower than 1.8 V, which can damage the cycling stability of Li-S battery.^{12, 13} As the use of inorganic separator is capable of circumventing the shuttle effect, the LiNO_3 is expected to be removed from the electrolyte. Fig. S23a shows the cycle performance of LLZTO and PP based batteries without the LiNO_3 additive. The LLZTO-based Li-S battery shows an initial discharge capacity of 1250 mA h g^{-1} with a Coulombic efficiency of 86 %. Then, after several cycles, the Coulombic efficiency of

LLZTO-battery rises and maintains at above 92 % in the subsequent cycles. However, the PP-based battery exhibits a discharge capacity of 960 mA h g⁻¹ and a charge capacity up to 1888 mA h g⁻¹, which is higher than the sulfur's theoretical specific capacity (1675 mA h g⁻¹), corresponding to a quite low Coulombic efficiency of 50.8 %. The severe overcharge phenomenon is also vividly observed from the charge-discharge curves (Fig. S23b). This poor performance is caused by severe polysulfide shuttle effect. By contrast, the LLZTO-based battery holds a higher Coulombic efficiency, indicating the polysulfide shuttle has been pronouncedly suppressed in LLZTO-based battery. Fig. S23c compares the charge-discharge profiles of the above two batteries. The PP-based battery presents a large time difference between charge and discharge in each cycle, which is caused by the serious polysulfide shuttle. As expected, the LLZTO-based battery shows almost symmetric charge-discharge curves, contributed by the suppressive shuttle effect.

Table S1. Electrochemical performance comparisons of previously reported Li-S battery and our presented case.

Ceramic ^{Ref.}	Sulfur loading	Rate/cycle N./Decay (per cycle)	Highest rate/Capacity (mAh g ⁻¹)
LATP ¹⁴	0.2 M Li ₂ S	0.05 C/150/0.017 %	0.5 C/512 (40 °C), 875 (50 °C)
LAGP ¹⁵	1 mg cm ⁻²	0.5 C/40/1.2 %	0.5 C/1341
LYZP ¹⁶	1.5 M S	0.2 C/150/0.07 %	0.5 C/780
LATP ¹⁷	2 mM Li ₂ S ₆	0.1 C/50/0.57 %	0.1 C/978
LATP ¹⁸	4 M S	C/3 /300/0.19 %	C/3 /~1000
LAGP ¹⁹	1 mg cm ⁻²	0.5 C/300/0.011 %	0.5 C/725
LAGP ²⁰	1 mg cm ⁻²	1 C/1200/0.022 %	1 C/570
Our work	LLZTO	0.5 C/500/0.034 %	2 C/403
	Al ₂ O ₃	1 mg cm ⁻²	0.5 C/450/0.064 %
	YSZ		0.5 C/450/0.064 %

References

1. Y. Li, Z. Wang, C. Li, Y. Cao, X. Guo, *J. Power Sources* **2014**, *248*, 642.
2. Y. Li, Y. Cao, X. Guo, *Solid State Ionics* **2013**, *253*, 76.
3. W. Xia, B. Xu, H. Duan, Y. Guo, H. Kang, H. Li and H. Liu, *ACS Appl. Mater. Inter.*, 2016, *8*, 5335.
4. Y. Jin and P. J. McGinn, *J. Power Sources*, 2013, *239*, 326.
5. W. Xia, B. Xu, H. Duan, X. Tang, Y. Guo, H. Kang, H. Li and H. Liu, *J. Am. Ceram. Soc.*, 2017, *100*, 2832.
6. Z. F. Yow, Y. L. Oh, W. Gu, R. P. Rao and S. Adams, *Solid State Ionics*, 2016, *292*, 122.
7. L. Ji, M. Rao, H. Zheng, L. Zhang, Y. Li, W. Duan, J. Guo, E. J. Cairns and Y. Zhang, *J. Am. Chem. Soc.*, 2011, *133*, 18522.
8. J. Gou, H. Zhang, X. Yang, Y. Chen, Y. Yu, X. Li, H. Zhang, *Adv. Funct. Mater.* **2018**, *28*, 1707272.
9. J. Xie, H. J. Peng, J. Q. Huang, W. T. Xu, X. Chen, Q. Zhang, *Angew Chem, Int. Ed.* **2017**, *129*, 16441.
10. T. Chen, Z. Zhang, B. Cheng, R. Chen, Y. Hu, L. Ma, G. Zhu, J. Liu, Z. Jin, *J. Am. Chem. Soc.* **2017**, *139*, 12710.
11. X. B. Cheng, H. J. Peng, J. Q. Huang, R. Zhang, C. Z. Zhao, Q. Zhang, *ACS Nano* **2015**, *9*, 6373.
12. S. S. Zhang, *J. Power Sources* **2016**, *322*, 99.
13. S. S. Zhang, *J. Electrochem. Soc.* **2012**, *159*, A920.
14. L. Wang, Y. Wang, Y. Xia, *Energy Environ. Sci.* **2015**, *8*, 1551.

15. Q. Wang, J. Jin, X. Wu, G. Ma, J. Yang, Z. Wen, *Phys. Chem. Chem. Phys.* **2014**, *16*, 21225.
16. X. Yu, Z. Bi, F. Zhao, A. Manthiram, *Adv. Energy Mater.* **2016**, *6*, 1601392.
17. S. Wang, Y. Ding, G. Zhou, G. Yu, A. Manthiram, *ACS Energy Lett.* **2016**, *1*, 1080.
18. X. Yu, Z. Bi, F. Zhao, , A. Manthiram *ACS Appl. Mater. Inter*, **2015**, *7*, 16625.
19. Q. Wang, Z. Wen, J. Jin, J. Guo, X. Huang, J. Yang, C. Chen, *Chem. Commun.* **2016**, *52*, 1637.
20. S. Gu, X. Huang, Q. Wang, J. Jin, Q. Wang, Z. Wen, R. Qian, *J. Mater. Chem. A* **2017**, *5*, 13971.